nature communications

Article

https://doi.org/10.1038/s41467-025-63350-0

Auto-oscillations and directional magnon emission induced by spin current injection into large magnetic volumes

Received: 9 February 2025

Accepted: 18 August 2025

Published online: 26 September 2025

Check for updates

Richard Schlitz[1,2] ✉, Vladislav E. Demidov[3], Michaela Lammel[2], Sergej O. Demokritov[3] & Pietro Gambardella[1]

The ability to manipulate magnons using electronic currents holds transformative potential for high-frequency signal processing architectures based on insulating magnetic materials. A critical challenge, however, lies in achieving efficient magnon emission and amplification through damping compensation, which typically requires ultra-thin films. In this study, we break this limitation by demonstrating a three-order-of-magnitude increase in magnon population, consistent with the onset of auto-oscillations upon reaching damping compensation, by injecting a spin current from a µm-wide Pt wire into a continuous 150 nm-thick yttrium iron garnet film. Using nonlocal magnon transport and Brillouin light scattering, we reveal that damping compensation occurs due to magnon self-localization beneath the Pt injector, which precludes radiation from the excited region. As a result, the nonlocal magnon conductance becomes mode-dependent and is significantly amplified by multi-magnon scattering at high magnon populations. Finally, we demonstrate that interfacial spin injection breaks yttrium iron garnet's inversion symmetry, leading to unidirectional magnon emission. Our results pave the way for the development of advanced magnonic devices, including directional magnon emitters, and offer a new approach to achieving damping compensation in thick magnetic films.

Magnons are quantized excitations of ordered magnetic systems that carry spin angular momentum and can propagate coherently over millimeter-scale distances without the energy loss associated with charge motion. This characteristic makes them promising as alternative information carriers in insulating materials, enabling novel wave-based computing architectures[1–5]. A key advantage of magnons, unlike phonons and photons, is their strong mutual interactions, leading to pronounced nonlinear behavior. Understanding and harnessing this nonlinear behavior is essential for developing efficient magnonic devices.

Magnonic systems operating in the nonlinear regime offer enhanced functionalities, including parametric spin wave amplification[6], frequency conversion[7], and frequency comb generation[8–10]. Furthermore, the large magnon populations obtained in the nonlinear regime inherently promote multi-magnon scattering processes[11–13] and lead to phenomena such as magnon Bose–Einstein condensation[4,14], foldover instabilities[15,16] and nonlinear frequency shifts[17,18].

While conventional excitation schemes for magnons rely on GHz electromagnetic fields, recent works leverage electronic spin currents for magnon excitation[3,19–21]. Such spin currents can be straightforwardly generated by using charge to spin conversion via the spin Hall effect in a metal with strong spin-orbit coupling interfaced with the magnetic layer (Fig. 1a–c)[21–23]. Injecting large spin currents into a

[1]Department of Materials, ETH Zurich, Zurich, Switzerland. [2]Department of Physics, University of Konstanz, Konstanz, Germany. [3]Institute of Applied Physics, University of Muenster, Muenster, Germany. ✉e-mail: richard.schlitz@uni-konstanz.de

https://doi.org/10.1038/s41467-025-63350-0

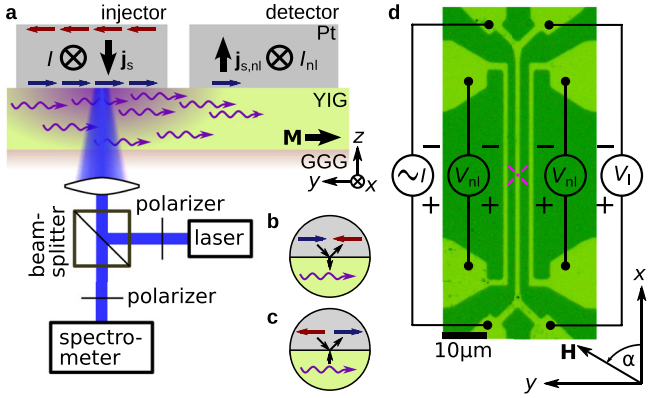

Fig. 1 | Schematic of the experiment. a cross-section of the nonlocal device. A current *I* flowing in a Pt wire (injector) induces a spin accumulation via the spin Hall effect at the interface with YIG, which leads to the nonequilibrium injection of magnons in YIG. This magnon accumulation (carrying a spin angular momentum represented by the direction of the wavy arrow) can either be detected electrically by a second Pt electrode (detector) or optically via BLS. **b, c** Magnons can be created or annihilated, respectively, by the electronic spin accumulation at the interface via exchange coupling between the Pt and Fe atoms in the YIG layer. **d** Optical micrograph of the investigated device with contact scheme and coordinate system. The magenta cross marks the position of the laser spot used for the BLS measurements.

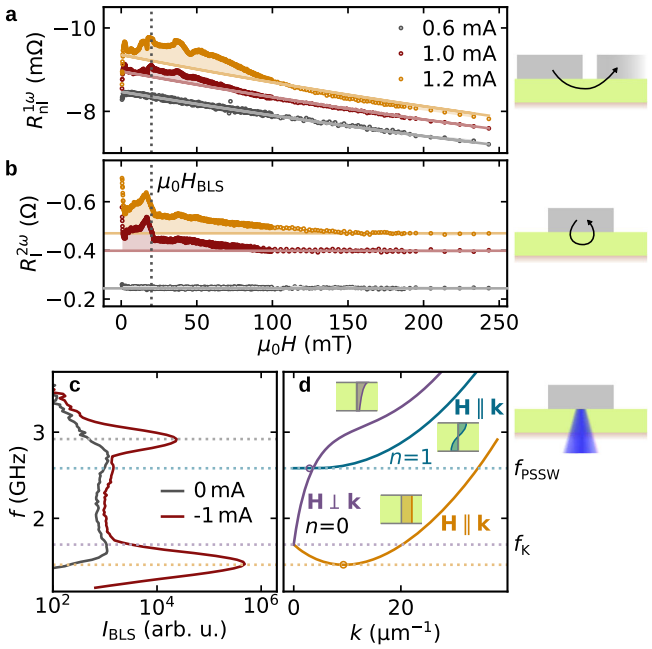

Fig. 2 | Evidence for magnetic auto-oscillations in a 150-nm-thick YIG layer. **a** Nonlocal resistance vs magnetic field applied at an angle $\alpha = 90°$ of a device with injector-detector separation $d = 3$ μm measured in the linear (gray) and nonlinear (red and yellow) regime. The current in the legend refers to the zero-to-peak current amplitude I_{ac}. **b** Second harmonic local resistance of the injector recorded simultaneously with the nonlocal resistance of the detector. The vertical gray dotted line marks the magnetic field applied during the BLS measurement shown in (**c**). The solid lines are fits to the field dependence in the linear regime (see supplementary information). **c** BLS measurement of the magnon occupation in thermal equilibrium (gray) and with nonlinear magnon excitation by spin current injection (red). The magnetic field $\mu_0 H = 20$ mT was applied at $\alpha = 270°$. The BLS spectra were recorded while applying the dc current I_{dc} specified in the legend. **d** Calculated dispersion of the first two magnon branches. The insets show the mode profile across the thickness of the YIG film.

magnetic film gives rise to a pronounced nonlinear behavior, where the mode population at the bottom of the magnon band is drastically enhanced[21,24]. Further tailoring the magnetic anisotropy to reduce nonlinear relaxation pathways[21,25] enables the condensation of magnons into a single coherent state[26–28]. In addition to tailoring the anisotropy of the magnetic layer, adding metallic overlayers can lead to a shift of the magnon dispersion by increasing damping or interfacial anisotropy, providing a way to locally tailor the magnon dispersion[29,30].

Despite these impressive achievements, the excitation of coherent magnons required for most applications remains a difficult task[24,31,32]. Overcoming this limitation is possible when the amount of injected angular momentum becomes comparable to the total spin moment in the magnetic volume of the film, and thus for sufficiently thin magnetic films with low damping, typically yttrium iron garnet (YIG) with thickness $\lesssim$30 nm. Achieving damping compensation in thicker magnetic films would significantly expand the range of devices and magnonic effects that can be exploited via electrical spin injection. Thick films additionally support multiple magnon modes, opening up opportunities for novel nonlinear effects. However, the large magnetic volume and the interfacial nature of spin injection present yet unresolved challenges for achieving sufficiently large magnon populations in these thicker films.

In this work, we demonstrate damping compensation in 150 nm-thick YIG magnetic layers with uncompensated anisotropy, facilitated by self-localization of excited magnons beneath the spin current injector. This effect leads to auto-oscillations of the magnetization, evident by a three-order-of-magnitude increase in magnon population near the bottom of the magnon spectrum. Through Brillouin light scattering (BLS) and nonlocal magnon transport analysis, we reveal interference effects that modify the magnon conductance and determine the sensitivity of nonlocal transport to specific magnon modes. Our findings also show that the spatial modulation of the magnon dispersion, combined with mode-dependent nonlinear scattering processes, results in pronounced unidirectional magnon emission from the excitation region, allowing for efficient on-chip microwave sourcing. These phenomena enable dynamic control over magnon populations, propagation, and energy transfer among different magnon modes, highlighting the potential of thick magnetic layers for integration in magnonic devices.

Results

Device and experimental principle

The device schematic and measurement setup are shown in Fig. 1. The device consists of three parallel Pt wires deposited on a 150 nm-thick YIG layer grown by liquid phase epitaxy on a $Gd_3Ga_5O_{12}$ substrate. The center-to-center separation and width of each wire are 3.0 μm and 1.1 μm, respectively. To study the local and nonlocal magnon transport[20,33–36], we apply an alternate current of peak amplitude I_{ac} and frequency $\omega/2\pi = 10$ Hz in the central (injector) wire and measure the first harmonic of the nonlocal voltage $V_{nl}^{1\omega}$ at the two outer (detector) wires. Hereby, the current is converted to a spin current in the injector by the spin Hall effect, generating magnons by interfacial exchange coupling (Fig. 1b, c), which propagate through the YIG layer and are subsequently detected via the inverse spin Hall effect in the detector. The first harmonic nonlocal resistance, defined as $R_{nl}^{1\omega} = V_{nl}^{1\omega}/I$, is directly proportional to the total number of nonequilibrium magnons below the detector, irrespective of their phase, energy or wave vector[34]. Additionally, we measure the second harmonic local resistance $R_I^{2\omega} = V_I^{2\omega}/I$ using a four-point probe of the voltage drop $V_I^{2\omega}$ across the central wire (see methods). The latter contains contributions from the spin Seebeck effect[37,38] and the magnetoresistances arising from the creation or annihilation of magnons[39]. $R_I^{2\omega}$ thereby reveals the magnon accumulation below the injector wire (cf. sketch right of Fig. 2b)[39]. The nonlocal magnon transport measurements are complemented by microfocus BLS spectroscopy[40], which allows us to gather spectral information on the magnon accumulation below the injector wire.

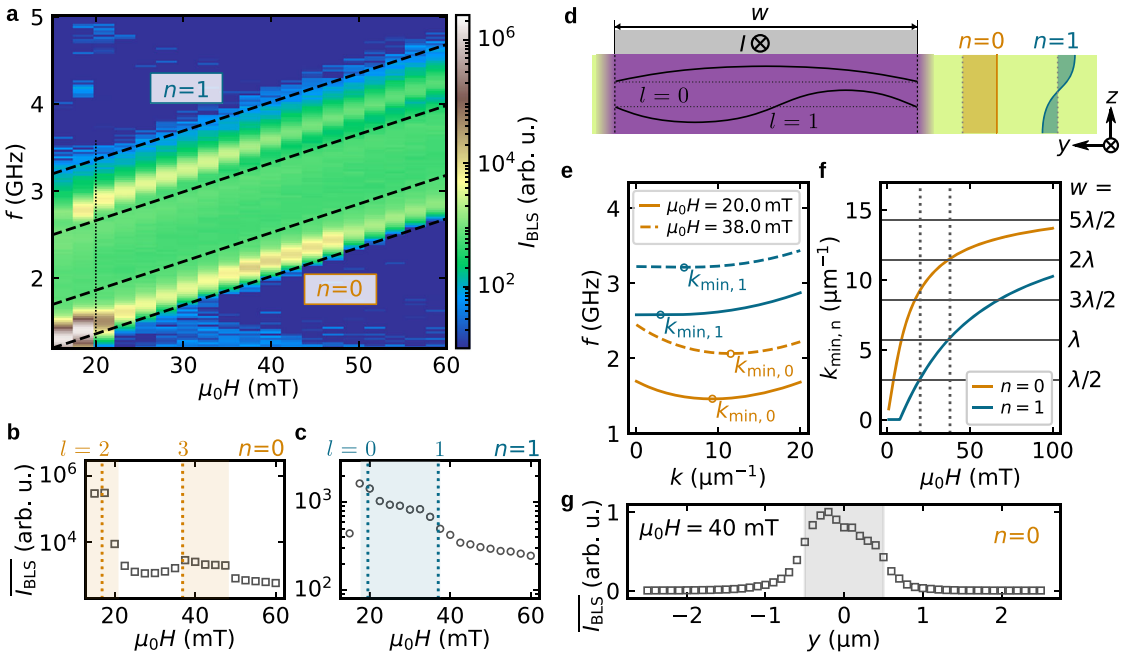

Fig. 3 | Dependence of the magnon population on magnetic field. a Map of the BLS intensity as a function of f and $\mu_0 H$. The two pairs of dashed lines mark the spectral ranges used for integration in (**b**) and (**c**). The thin dotted line marks the line cut shown in Fig. 2d. **b**, **c** BLS intensity integrated within the two bounds marked by the dashed lines in (**a**), corresponding to the occupancy of the $n = 0$ mode (**b**) and the $n = 1$ mode (**c**). The dotted vertical lines identify the mode order/ (see **d**–**f**). The orange and teal shaded regions mark the range of enhanced BLS contrast. **d** Schematic cut through the sample. When applying a current in Pt, magnons are confined below the central wire due to the nonlinear frequency shift (purple shading). Consequently, standing wave patterns (black lines) emerge. The vertical mode profile of the lowest two magnon branches is depicted by the orange ($n = 0$) and teal ($n = 1$) lines on the right. **e** Calculated dispersion of the two lowest magnon branches shows that the wave vector k_{min} of the band minimum shifts with magnetic field. **f** Position k_{min} as a function of magnetic field. Constructive interference occurs when $k_{min,n} = (l + 1)\pi/w$ (see **d**). The vertical dotted lines correspond to the two magnetic fields shown in (**e**). **g** BLS signal integrated under the $n = 0$ peak recorded while scanning the laser spot across the injector wire (gray shaded region). The trace has been normalized to its maximum value. All data in the figure were recorded at a dc current of $I_{dc} = -1$ mA and with the magnetic field applied at $\alpha = 270°$.

Damping compensation due to magnon self-localization

Figure 2a, b shows $R_{nl}^{1\omega}$ and $R_{I}^{2\omega}$ recorded during a magnetic field sweep at different currents. In the linear regime (gray symbols), $R_{nl}^{1\omega}$ decays due to the reduction of the magnon diffusion length at high magnetic field[41,42] (see discussion in Supplementary Note 1). $R_{I}^{2\omega}$, on the other hand, is constant in the entire field range, indicating that the local signal is dominated by the spin Seebeck effect[39]. In the nonlinear regime (red and orange symbols), both $R_{nl}^{1\omega}$ and $R_{I}^{2\omega}$ exhibit strongly nonmonotonic field-dependent features, which we assign to the excitation of different magnon modes beneath the detector and injector, respectively. The nonlinear regime is reached for currents around 0.7 mA, corresponding to a critical current density of $j_c \approx 1.6 \times 10^{11}$ A m^{-2} (see Supplementary Fig.2).

To further establish the situation below the injector, we use BLS to probe changes in the magnon population induced by driving the YIG film into the nonlinear regime. Fig. 2c shows the BLS spectra recorded at the position marked by the magenta cross in Fig. 1d. At zero current (gray line), the occupied mode spectrum has two characteristic peaks, one close to the Kittel frequency f_K and one close to the first perpendicular standing spin wave (PSSW, $n = 1$) mode f_{PSSW}, as calculated for a 150 nm thick YIG film (dotted lines). The dispersion of these modes is shown in Fig. 2d, together with the Damon–Eschbach (DE) and backward volume (BV) branches of the $n = 0$ mode with wave vectors $\mathbf{k} \perp \mathbf{H}$ and $\mathbf{k} \parallel \mathbf{H}$, respectively. At a current of −1 mA, the system is driven in the nonlinear regime, resulting in a drastic increase in the BLS intensity, as shown by the red curve in Fig. 2c (note the logarithmic scale). The BLS signal that corresponds to the minimum of the magnon band is enhanced by three orders of magnitude, indicating the onset of auto-oscillations. Moreover, the PSSW mode appears to be shifted to higher frequencies, likely due to the current-dependent spin pumping at the insulator–metal interface[30].

The observation of auto-oscillations in such a thick YIG film is highly peculiar. Typically, a large film thickness is expected to inhibit auto-oscillations because the injected spin current through the interface is insufficient to compensate for the damping across the entire layer. Additionally, the open geometry and uncompensated ellipticity of the precession, favoring radiation and strong nonlinear relaxation effects, should prohibit large mode populations[21].

We attribute the ability to reach the auto-oscillation threshold, despite the factors typically limiting it, to a spatially varying modification of the magnon dispersion caused by a nonlinear frequency shift of the local magnon band (evident also in current-dependent BLS measurements shown in Supplementary Fig. 3). This modification effectively confines the excited magnons to the region directly beneath the injector. Such a nonlinear frequency shift can arise due to the reduction of magnetization by local heating, a high density of electrically excited magnons in the driven region, or a local modification of the magnon lifetime[15,30,43–45]. The lack of compatible magnon modes in the YIG region outside the injector limits magnon radiation, which in turn allows for a higher occupancy of magnons within the confinement region.

Local interference effects

If the auto-oscillations result from mode confinement below the injector, interference effects[46,47] are expected when the magnon wave vector matches the width of the confinement region[29]. To confirm this notion, we analyze the dispersion of the low-energy magnon spectrum using BLS in Fig. 3a. We observe an oscillation of the intensity of both modes when changing the magnetic field. Integrating the BLS intensity

of the two modes in a narrow frequency range confirms this notion (cf. Fig. 3b, c). To understand this behavior, we consider a cross-section of the device (see Fig. 3d). If the region below the injector forms a potential well, reflections of the magnons at either interface become possible, and standing waves will form. The requirement for constructive interference is a magnon wavelength $\lambda = 2w/(l+1)$, where w is the width of the Pt wire. The wave vector of the band minimum k_{min} shifts with the magnetic field (cf. Fig. 3e) for both BV branches and can be extracted from the spectrum for a range of magnetic fields as shown in Fig. 3f. The magnetic fields at which the magnons at the band minimum fulfill the resonance condition $\lambda = 2\pi/k_{min}$ are marked by dotted vertical lines in Fig. 3b, c for the $n = 0$ and $n = 1$ branch, respectively. Comparing these dotted lines to the integrated intensity of the two modes in Fig. 3b, c, we find reasonable agreement. To experimentally confirm the localization of magnons below the injector when the resonance condition is fulfilled, we record the integral BLS intensity under the $n = 0$ peak as a function of the laser spot position (see Fig. 3g). The rapid exponential decay of the magnons in the YIG region outside of the Pt wire is consistent with the transient decay of the localized low-energy magnons. The field-dependent oscillations and direct observation of the transient magnon decay corroborate the key role of self-localization and the consequent enhancement by interference in the appearance of auto-oscillations despite the large thickness of our YIG layer.

Signatures of magnon interference and mode-dependent emission in electric transport

Electrical measurements of magnon transport in thin-film YIG by spin currents typically do not yield information on the excited modes[48]. Here, we show that magnon interference effects result in mode-dependent local and nonlocal transport characteristics, highlighting the possibility of obtaining information on excited modes. Figure 4a shows that the intensity oscillations of $R_{\mathrm{I}}^{2\omega}$ as a function of magnetic field correspond to the resonant conditions for the (n, l) standing wave modes. The $n = 0$ mode, having the highest occupancy, appears most prominently in $R_{\mathrm{I}}^{2\omega}$. The relative intensity of the (0, l) peaks is influenced by the inhomogeneous broadening of the mode linewidth at low magnetic fields (see broadband ferromagnetic resonance measurements in Supplementary Fig. 4). This broadening reduces the spatial coherence of the modes, thereby diminishing the intensity of the peaks as the field decreases. The nonlocal $R_{\mathrm{nl}}^{1\omega}$, shown in Fig. 4b, exhibits a more complex dependence on the standing wave condition, with local minima observed in correspondence with the (0, l) modes and maxima for the (1, l) modes. This complex behavior can be attributed to counteracting effects. On the one hand, a higher local magnon population beneath the injector leads to an enhanced nonlocal signal due to the increase in nonlinear relaxation and corresponding outward magnon radiation. On the other hand, exactly fulfilling the standing wave condition of the $n = 0$ modes leads to a lower nonlocal signal due to the more efficient localization of the modes. This effect is particularly pronounced at lower magnetic fields, where the spatial confinement is stronger. Figure 4c illustrates how the propagation of the $n = 0$ modes close to the band bottom is suppressed when the large magnon occupation leads to a strong nonlinear frequency shift of the dispersion below the injector. In this situation, outward magnon radiation is inhibited by the frequency mismatch with the gapped magnon states outside the injector.

The situation is different for the $n = 1$ modes. In this case, four magnon scattering processes[12,13] as shown in Fig. 4d can efficiently excite magnons in the $n = 0$ magnon branch, leading to enhanced emission of magnons with large group velocities that lie above the gapped frequency region. Accordingly, we observe that $R_{\mathrm{nl}}^{1\omega}$ is enhanced when the $n = 1$ modes are resonantly enhanced by interference (Fig. 4b). The magnons generated by four-magnon scattering additionally should have a high group velocity and consequently a long

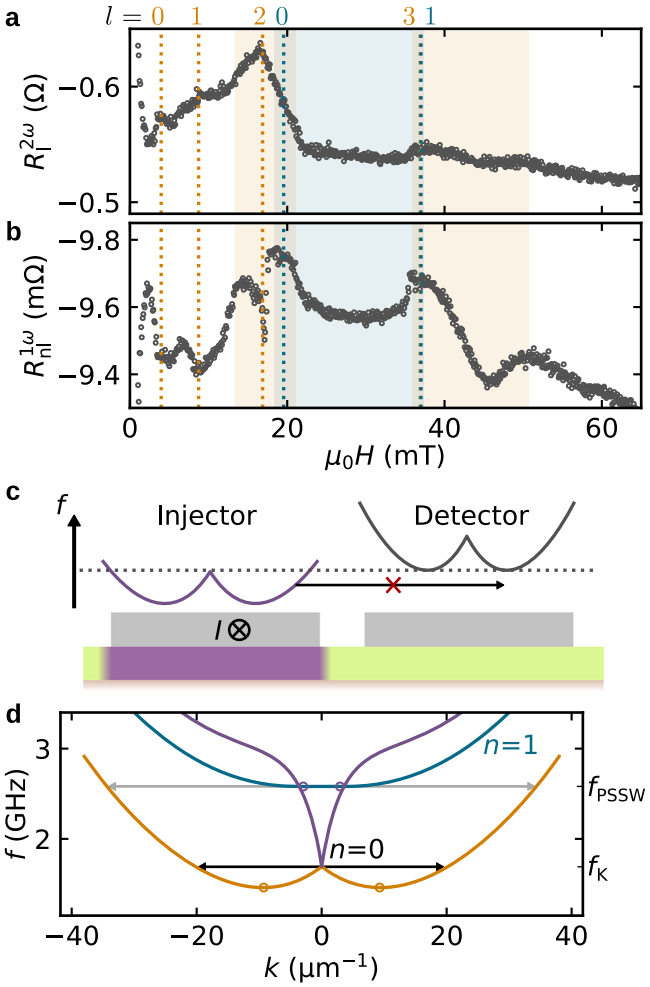

Fig. 4 | Enhanced magnon emission by four-magnon scattering. a, b $R_{\mathrm{I}}^{2\omega}$ and $R_{\mathrm{nl}}^{1\omega}$ as a function of magnetic field recorded at $I_{ac} = 1.2$ mA in the nonlinear regime (zoom of the orange traces in Fig. 2a, b). The dotted lines correspond to the standing wave conditions of the $n = 0$ mode (orange) and the $n = 1$ mode (teal). The shaded regions mark the field range with enhanced BLS contrast (see Fig. 3b, c) for the $n = 0$ mode (orange) and $n = 1$ mode (teal). **c** Schematic magnon dispersion below the injector and detector. The reduced magnetization in the nonequilibrium region below the injector (purple) leads to a lowering of the magnon energy, here calculated for a magnetization reduced to 70% of the room temperature value. As a result, magnons close to the band minimum cannot propagate out of the nonequilibrium region except via nonlinear processes. **d** Four magnon scattering within the $n = 0$ band (black arrows) can efficiently excite propagating modes. Four magnon scattering from the $n = 1$ band to the $n = 0$ band (gray arrows) with energy degenerate modes leads to efficient radiation of $n = 1$ magnons.

propagation distance, as confirmed by distance-dependent transport measurements (see Supplementary Fig. 5)

We note that our simple model does not capture the local changes of the magnon dispersion induced by heating and mode hybridization. As a consequence, the exact shape of the peaks observed in the BLS and transport measurements is difficult to predict. Nevertheless, the model allows to explain the key features and resonances, also for devices with different wire widths (see Supplementary Fig. 6), confirming its general applicability. Additionally, the presence of similar features in many different devices emphasizes that local variations of the YIG film cannot be the determining factor in the generation of the nonlinear response, in line with the small inhomogeneous broadening observed in the ferromagnetic resonance measurements (Supplementary Fig. 4). Our data thus demonstrate that individual magnon modes and their occupation have a pronounced impact on nonlocal

magnon transport, which is determined by the interplay between localized mode confinement and nonlinear relaxation processes.

Unidirectional magnon emission

Magnons are an attractive platform for devices with pronounced nonreciprocal behavior[49–51]. Recent studies have revealed that the magnon propagation velocity is asymmetric in thin-film YIG due to the interfacial Dzyaloshinsky-Moriya interaction (DMI) induced by interfacial symmetry breaking[52,53]. In thick YIG films, however, the DMI becomes less significant due to the diminished influence of the interface relative to the bulk. Consequently, achieving sizable directional magnon emission in YIG films thicker than 50 nm appears to be challenging[53]. In the following, we demonstrate that interfacial spin injection in the nonlinear regime provides a powerful symmetry-breaking mechanism that induces directional magnon emission independent of the DMI.

To isolate directional contributions in the nonlocal transport measurements, we measure the difference $\Delta R_{\mathrm{nl}}^{1\omega} = (R_{\mathrm{nl,L}}^{1\omega} - R_{\mathrm{nl,R}}^{1\omega})/2$ of the nonlocal resistance of the left and the right electrodes (cf. Fig. 5a). In Fig. 5b, c, we show $\Delta R_{\mathrm{nl}}^{1\omega}$ normalized to the average nonlocal resistance $\Sigma R_{\mathrm{nl}}^{1\omega} = (R_{\mathrm{nl,L}}^{1\omega} + R_{\mathrm{nl,R}}^{1\omega})/2$ (the raw data are shown in Supplementary Fig. 7)[53]. Owing to time-reversal symmetry, transport asymmetry in magnon propagation can only be observed when the magnons travel perpendicular to the magnetization direction. In our geometry, this requires wave vectors $\pm k_\perp$ perpendicular to the magnetization to have a component along y (cf. Fig. 5c). To eliminate constant asymmetry effects originating from geometric imperfections or lithographic inconsistencies in the placement of the two wires, we first measure $\Delta R_{\mathrm{nl}}^{1\omega}/\Sigma R_{\mathrm{nl}}^{1\omega}$ with the magnetic field aligned to the current-induced spin accumulation (along y), ensuring $k_\perp$ aligns along x. This measurement, shown in Fig. 5b, reveals a constant baseline with a sharp dip-peak feature near 18 mT. This field corresponds to the crossing of the minimum of the $n = 1$ branch and the $n = 0$ branch, with wave vectors $k = \pm k_\perp$ (cf. Fig. 4d). The resulting hybrid mode[54] inherits an asymmetric amplitude along the thickness of the YIG layer from the $k_\perp$ branch (cf. Fig. 5a), allowing for asymmetric magnon propagation close to the mode crossing. With the baseline established, we measure $\Delta R_{\mathrm{nl}}^{1\omega}/\Sigma R_{\mathrm{nl}}^{1\omega}$ with the magnetic field oriented at 72° from the x-axis, resulting in a finite component of $k_\perp$ along y. The results, shown in Fig. 5c, reveal a major enhancement in the directional asymmetry, which is strongly dependent on the magnetic field and reaches up to 5% of the total magnon emission. This asymmetry is opposite in sign and exceeds by one order of magnitude the one observed in linear response (0.5% for this sample) and attributed to the interfacial DMI[53] (see also supplementary information). Furthermore, by orienting the magnetic field at 108°, thereby inverting the projection of $k_\perp$ along y, the asymmetry inverts about the baseline, consistent with symmetry considerations.

To illustrate the mechanism of directional magnon emission, we consider the strong nonlinear decay of magnons from the $n = 1$ branch into the $n = 0$ branch observed at large injection currents (cf. Fig. 4b, d), which leads to a large occupation of magnons in the $n = 0$ branch with $k = k_\perp$. Such a relaxation channel dominates over the relaxation into the modes with $k_\parallel$ because the mode overlap between the $n = 1$ and $n = 0$ modes is the largest there. Additionally, this relaxation channel requires only magnons from one band minimum (either $\pm k_{\mathrm{min}}$) to conserve linear momentum and energy (cf. Fig. 5d). The amplitude profile of the $k = k_\perp$ mode is spatially inhomogeneous across the thickness of the YIG layer, and is inverted for opposite wave vectors, as sketched in Fig. 5a. Consequently, a difference in propagation for the $n = 0$ modes with $k_\perp \lesseqgtr 0$ arises when the inversion symmetry is broken along z. In our case, the strong upshift of the $n = 1$ mode observed in Fig. 2e, consistent with an effective reduction of the YIG thickness, suggests that inversion symmetry is broken by interfacial spin injection in the nonlinear regime. The nonequilibrium

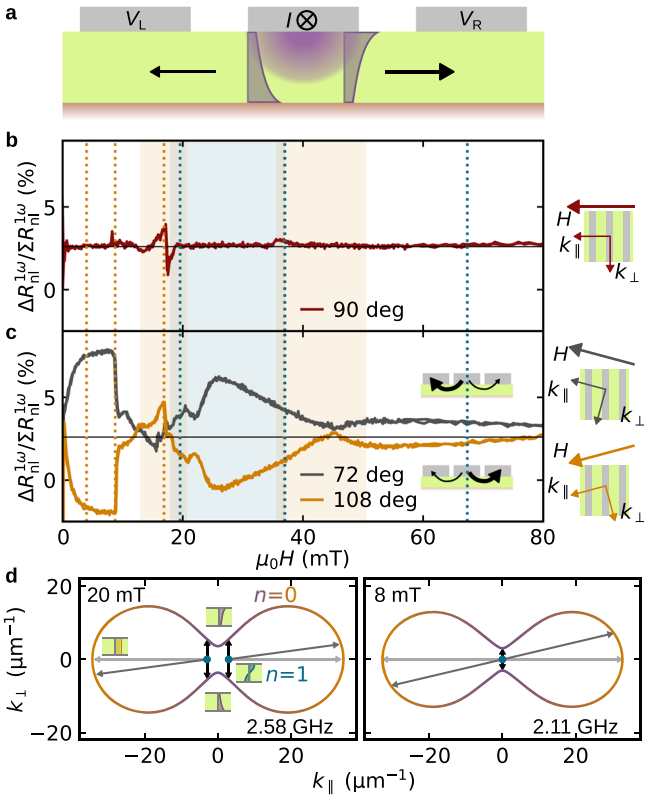

Fig. 5 | Directional magnon emission by spin injection and nonlinear relaxation. a Device cross-section with the mode profile of counter-propagating magnons from the DE branch (dark gray). The nonequilibrium region in the nonlinear regime below the injector (purple) is inhomogeneous across the film thickness, leading to symmetry-breaking and different amplitudes of counter-propagating DE magnons. Asymmetry of the nonlocal magnon resistance when the magnetic field is aligned with the spin accumulation and transport direction y (**b**) or at an angle of 72 and 108° with respect to x (±18° with respect to y) (**c**). $k_\perp$ and $k_\parallel$ wave vector components with respect to the device for the three orientations of the magnetic field are shown on the right. The dotted vertical lines correspond to the locations of the resonance condition (cf. Fig. 4a). The measurements are taken with a current $I_{\mathrm{ac}} = 1.2$ mA. The shaded regions mark the field range with enhanced BLS contrast (see Fig. 3b, c) for the $n = 0$ mode (orange) and $n = 1$ mode (teal). **d** Constant-energy cuts through the magnon dispersion at the energy of the band minimum of the $n = 1$ branch ($f = 2.58$ GHz and 2.11 GHz) calculated for $\mu_0 H = 20$ mT and 8 mT, respectively. The insets depict the mode profile across the YIG thickness. The two pairs of black arrows mark the dominant four magnon relaxation pathways from the $n = 1$ branch into the $n = 0$ branch. The gray arrows show four alternative magnon relaxation paths that require magnons from both minima.

nature of the symmetry breaking is further corroborated by the opposite sign of $\Delta R_{\mathrm{nl}}^{1\omega}/\Sigma R_{\mathrm{nl}}^{1\omega}$ when compared to the linear response regime (see Supplementary Note 2). This symmetry breaking thus enables in-situ control over the degree of directional emission from a nonequilibrium region, without requiring intrinsic symmetry breaking within the material, e.g., by interfacial DMI[55].

The field dependence of $\Delta R_{\mathrm{nl}}^{1\omega}/\Sigma R_{\mathrm{nl}}^{1\omega}$ further shows that directional emission is most pronounced below 10 mT, where the $n = 1$ mode has a minimal energy at $k = 0$ (see right panel in Fig. 5d), where the four magnon scattering can effectively excite magnon pairs across the entire constant energy cut of the $n = 0$ mode while conserving linear momentum. At $\mu_0 H \sim 16$ mT, $\Delta R_{\mathrm{nl}}^{1\omega}/\Sigma R_{\mathrm{nl}}^{1\omega}$ changes sign, which we associate with the hybridization of the $n = 0$ and $n = 1$ branches, leading to a strong modification of the dispersion. Between 20 and 40 mT, the wavevector of the $n = 1$ band minimum fulfills the resonance condition, so that the correspondingly higher mode population and thus more efficient nonlinear relaxation gives rise to an enhanced emission of

magnons with $k = k_{\perp}$. Above 40 mT, the directional component suggests another increase of the $n = 1$ occupation in the vicinity of the expected $l = 2$ resonance. At even larger fields, the system gradually returns to the linear regime due to the increase of the intrinsic magnon relaxation (cf. Fig. 2). Our data thus consistently indicate that strong magnon injection and efficient nonlinear relaxation from the $n = 1$ into the $n = 0$ branch leads to directional magnon emission.

Discussion

Reaching auto-oscillations in thick YIG films extends the functionality and scalability of magnonic devices by leveraging key properties enabled by the increased film thickness. Thick YIG films host a rich magnon band structure, with multiple degenerate and higher-order modes contributing to the magnon dynamics. This expanded mode spectrum allows for access to a wider range of frequencies, enhanced nonlinear interactions such as interband multi-magnon scattering, and the exploration of novel phenomena linked to mode coupling and hybridization, which are less pronounced in thinner films. Our results reveal that the auto-oscillation threshold can be readily reached in 150 nm-thick YIG by interfacial spin current injection using µm-wide Pt wires. The large magnetic volume of thick YIG promotes the self-localization of magnons below the spin injector due to the spatially-inhomogeneous reduction of the magnetization and consequent downward frequency shift of the magnon bands. Interference effects induced by magnon confinement below the injector manifest themselves into strong mode- and field-dependent local and nonlocal resistances that reflect the formation of standing waves and magnon radiation enabled by nonlinear relaxation processes, respectively. Additionally, we show that directional magnon currents can be efficiently driven in thick YIG films where the influence of interfacial DMI is practically negligible. We speculate that the directional emission could originate from the localization of the nonlinearly excited magnons close to the YIG/Pt interface, resembling a vertical version of the lateral confinement. Alternatively, the asymmetric localization of the two counterpropagating DE modes could favor the population of only one DE mode in the nonlinear regime. Finally, a vertically varying magnon dispersion due to Joule heating[55] or nonlinear magnon creation could further contribute to the observed directional emission.

The versatility and effectiveness of nonlinear spin injection in thick YIG films provide novel mechanisms for controlling magnon emission and transport in magnonic devices, including directional emitters that allow direct flow of energy within magnonic circuits, integrated directional traveling wave amplifiers, and frequency multiplexers. Additionally, the efficiency of the inductive readout of the magnonic excitations is improved in thicker YIG films due to the higher number of excited spins. These features make thick YIG films advantageous for applications in signal processing, logic, and neuromorphic computing using magnons as information carriers. Besides the richer magnon structure and mode coupling processes, thick YIG films provide minimal damping, high power handling, and efficient coupling with external systems where maintaining coherence and uniformity across a wide area is important, such as radiofrequency antennas.

Methods

Sample fabrication

A 150 nm-thick $Y_3Fe_5O_{12}$ film grown by liquid phase epitaxy on a $Gd_3Ga_5O_{12}$ substrate (Matesy GmbH, Jena, Germany) was cleaned with piranha acid (H_2SO_4:H_2O_2 in a 1:1 volumetric ratio) for 45 s. Subsequently, it was annealed in an ultra-high vacuum sputtering chamber at 200 °C for 2 h and a 4 nm-thick layer of Pt was deposited at room temperature. The nonlocal devices were defined by Ar ion milling after masking with optical lithography and have a wire length and width of 120 µm and 1.1 µm, respectively. The center–center separation between the injector and the two outer wires is 3.0 µm.

Transport measurements

Transport measurements were performed at room temperature in an electromagnet. To measure the local and nonlocal resistance, we applied a sinusoidal current with frequency of 10 Hz and peak amplitude I_{ac} to the central wire and recorded the local and nonlocal voltage time traces that were subsequently demodulated to obtain the n-th harmonic components of the resistance $R^{n\omega} = V^{n\omega}/I_{ac}$ (for details see refs. 20,35,56). For the measurements of the directional components, the signal on the left and right wires was recorded simultaneously.

Micro-focus BLS measurements

The measurements were performed at room temperature. A DC current I_{dc} was applied to the central Pt wire. The probing light had a wavelength 473 nm and power of 0.25 mW and was generated by a single-frequency laser with spectral linewidth <10 MHz. The light was focused to a diffraction-limited spot with submicrometer size using a 100× aberration-corrected microscope with a 0.85 NA objective lens. The reflected light was analyzed by a six-pass Fabry-Perot interferometer.

Calculation of magnon spectra

Magnon spectra were calculated using the analytical model for dipole-exchange spin waves proposed in ref. 54, i.e., by combining Eqs. (A12), (A14), (45) and (46) therein. We used a spin wave stiffness of $\alpha = 3 \times 10^{-12}$ cm^2[57], a gyromagnetic ratio $\gamma = 28$ GHz T^{-1} and a saturation magnetization of $M_s = 130$ kA m^{-1} to account for the reduction of magnetization induced by the Joule heating. To obtain the resonance condition for standing wave formation below the injector, we determine the wave vector and energy minimum from the calculated spectra as a function of the applied magnetic field in the backward volume geometry.

Data availability

The data that support the findings of this study are available via the ETH Research Collection at https://doi.org/10.3929/ethz-b-000743320.

References

1. Chumak, A. V., Vasyuchka, V. I., Serga, A. A. & Hillebrands, B. Magnon spintronics. *Nat. Phys.* **11**, 453–461 (2015).
2. Neusser, S. & Grundler, D. Magnonics: spin waves on the nanoscale. *Adv. Mater.* **21**, 2927–2932 (2009).
3. Demidov, V. E. et al. Magnetization oscillations and waves driven by pure spin currents. *Phys. Rep.* **673**, 1–31 (2017).
4. Pirro, P., Vasyuchka, V. I., Serga, A. A. & Hillebrands, B. Advances in coherent magnonics. *Nat. Rev. Mater.* **6**, 1114–1135 (2021).
5. Chumak, A. V. et al. Advances in magnetics roadmap on spin-wave computing. *IEEE Trans. Magn.* **58**, 1–72 (2022).
6. Kolodin, P. A. et al. Amplification of microwave magnetic envelope solitons in thin yttrium iron garnet films by parallel pumping. *Phys. Rev. Lett.* **80**, 1976–1979 (1998).
7. Mohseni, M. et al. Controlling the nonlinear relaxation of quantized propagating magnons in nanodevices. *Phys. Rev. Lett.* **126**, 097202 (2021).
8. Wang, Z. et al. Magnonic frequency comb through nonlinear magnon-Skyrmion scattering. *Phys. Rev. Lett.* **127**, 037202 (2021).
9. Hula, T. et al. Spin-wave frequency combs. *Appl. Phys. Lett.* **121**, 112404 (2022).
10. Wang, C. et al. Enhancement of magnonic frequency combs by exceptional points. *Nat. Phys.* **20**, 1139–1144 (2024).
11. Gurevich, A.G., Melkov, G.A. *Magnetization Oscillations and Waves*, 1st edn. https://doi.org/10.1201/9780138748487 (CRC Press, 1996).
12. Schultheiss, H., Vogt, K. & Hillebrands, B. Direct observation of nonlinear four-magnon scattering in spin-wave microconduits. *Phys. Rev. B* **86**, 054414 (2012).

13. Sheng, L. et al. Nonlocal detection of interlayer three-magnon coupling. *Phys. Rev. Lett.* **130**, 046701 (2023).
14. Demokritov, S. O. et al. Bose-Einstein condensation of quasi-equilibrium magnons at room temperature under pumping. *Nature* **443**, 430–433 (2006).
15. Suhl, H. The theory of ferromagnetic resonance at high signal powers. *J. Phys. Chem. Solids* **1**, 209–227 (1957).
16. Seagle, D. J., Charap, S. H. & Artman, J. O. Foldover in YIG. *J. Appl. Phys.* **57**, 3706–3708 (1985).
17. Bauer, H. G., Majchrak, P., Kachel, T., Back, C. H. & Woltersdorf, G. Nonlinear spin-wave excitations at low magnetic bias fields. *Nat. Commun.* **6**, 8274 (2015).
18. Barsukov, I. et al. Giant nonlinear damping in nanoscale ferromagnets. *Sci. Adv.* **5**, 6943 (2019).
19. Demidov, V. E. et al. Magnetic nano-oscillator driven by pure spin current. *Nat. Mater.* **11**, 1028–1031 (2012).
20. Cornelissen, L. J., Liu, J., Duine, R. A., Youssef, J. B. & van Wees, B. J. Long-distance transport of magnon spin information in a magnetic insulator at room temperature. *Nat. Phys.* **11**, 1022–1026 (2015).
21. Demidov, V. E. et al. Spin-orbit-torque magnonics. *J. Appl. Phys.* **127**, 170901 (2020).
22. Sinova, J., Valenzuela, S. O., Wunderlich, J., Back, C. H. & Jungwirth, T. Spin Hall effects. *Rev. Mod. Phys.* **87**, 1213–1260 (2015).
23. Chen, T. et al. Spin-torque and spin-Hall nano-oscillators. *Proc. IEEE* **104**, 1919–1945 (2016).
24. Demidov, V. E., Urazhdin, S., Divinskiy, B., Bessonov, V. D., Rinkevich, A. B., Ustinov, V. V. & Demokritov, S. O. Chemical potential of quasi-equilibrium magnon gas driven by pure spin current. *Nat. Commun.* **8**, 1579 (2017).
25. Soumah, L. et al. Ultra-low-damping insulating magnetic thin films get perpendicular. *Nat. Commun.* **9**, 3355 (2018).
26. Divinskiy, B. et al. Evidence for spin current-driven Bose-Einstein condensation of magnons. *Nat. Commun.* **12**, 6541 (2021).
27. Merbouche, H. et al. True amplification of spin waves in magnonic nano-waveguides. *Nat. Commun.* **15**, 1560 (2024).
28. Frostad, T. et al. Anisotropy-assisted magnon condensation in ferromagnetic thin films. *Phys. Rev. Res.* **6**, 012011 (2024).
29. Santos, O. A. & Van Wees, B. J. Magnon confinement in an all-on-chip YIG cavity resonator using hybrid YIG/Py magnon barriers. *Nano Lett.* **23**, 9303–9309 (2023).
30. Lee, B. H., Fakhrul, T., Ross, C. A. & Beach, G. S. D. Large anomalous frequency shift in perpendicular standing spin wave modes in BiYIG films induced by thin metallic overlayers. *Phys. Rev. Lett.* **130**, 126703 (2023).
31. Takahashi, S., Saitoh, E. & Maekawa, S. Spin current through a normal-metal/insulating-ferromagnet junction. *J. Phys.Conf. Ser.* **200**, 062030 (2010).
32. Bender, S. A., Duine, R. A. & Tserkovnyak, Y. Electronic pumping of quasiequilibrium Bose-Einstein-condensed magnons. *Phys. Rev. Lett.* **108**, 246601 (2012).
33. Zhang, S. S.-L. & Zhang, S. Magnon-mediated electric current drag across a ferromagnetic insulator layer. *Phys. Rev. Lett.* **109**, 096603 (2012).
34. Zhang, S. S.-L. & Zhang, S. Spin convertance at magnetic interfaces. *Phys. Rev. B* **86**, 214424 (2012).
35. Goennenwein, S. T. B. et al. Non-local magnetoresistance in YIG/Pt nanostructures. *Appl. Phys. Lett.* **107**, 172405 (2015).
36. Althammer, M. All-electrical magnon transport experiments in magnetically ordered insulators. *Phys. Status Solidi Rapid Res. Lett.* **15**, 2100130 (2021).
37. Uchida, K.-I. et al. Observation of longitudinal spin-seebeck effect in magnetic insulators. *Appl. Phys. Lett.* **97**, 172505 (2010).
38. Kikkawa, T. & Saitoh, E. Spin Seebeck Effect: sensitive probe for elementary excitation, spin correlation, transport, magnetic order, and domains in solids. *Annu. Rev. Condens. Matter Phys.* **14**, 040721–014957 (2023).
39. Noël, P. et al. Nonlinear longitudinal and transverse magnetoresistances due to current-induced magnon creation-annihilation processes. *Phys. Rev. Lett.* **134**, 146701 (2025).
40. Demidov, V. E. & Demokritov, S. O. Magnonic waveguides studied by microfocus Brillouin light scattering. *IEEE Trans. Magn.* **51**, 1–15 (2015).
41. Cornelissen, L. J. & van Wees, B. J. Magnetic field dependence of the magnon spin diffusion length in the magnetic insulator yttrium iron garnet. *Phys. Rev. B* **93**, 020403 (2016).
42. Gückelhorn, J. et al. Magnon transport in Y3Fe5O12/Pt nanostructures with reduced effective magnetization. *Phys. Rev. B* **104**, 180410 (2021).
43. Suhl, H. Note on the saturation of the main resonance in ferromagnetics. *J. Appl. Phys.* **30**, 1961–1964 (1959).
44. Kohno, R. et al. Nonlocal magnon transconductance in extended magnetic insulating films. I. Spin diode effect. *Phys. Rev. B* **108**, 144410 (2023).
45. Kohno, R. et al. Nonlocal magnon transconductance in extended magnetic insulating films. II. Two-fluid behavior. *Phys. Rev. B* **108**, 144411 (2023).
46. Kendziorczyk, T., Demokritov, S. O. & Kuhn, T. Spin-wave-mediated mutual synchronization of spin-torque nano-oscillators: a micromagnetic study of multistable phase locking. *Phys. Rev. B* **90**, 054414 (2014).
47. Haidar, M. Interference patterns of propagating spin waves in spin-Hall oscillator arrays. *J. Appl. Phys.* **135**, 223901 (2024).
48. Cornelissen, L. J., Peters, K. J. H., Bauer, G. E. W., Duine, R. A. & van Wees, B. J. Magnon spin transport driven by the magnon chemical potential in a magnetic insulator. *Phys. Rev. B* **94**, 014412 (2016).
49. An, T. et al. Unidirectional spin-wave heat conveyer. *Nat. Mater.* **12**, 549–553 (2013).
50. Chen, J. et al. Excitation of unidirectional exchange spin waves by a nanoscale magnetic grating. *Phys. Rev. B* **100**, 104427 (2019).
51. Chen, J., Yu, H. & Gubbiotti, G. Unidirectional spin-wave propagation and devices. *J. Phys. D Appl. Phys.* **55**, 123001 (2022).
52. Wang, H. et al. Chiral spin-wave velocities induced by all-garnet interfacial Dzyaloshinskii-Moriya interaction in ultrathin yttrium iron garnet films. *Phys. Rev. Lett.* **124**, 027203 (2020).
53. Schlitz, R. et al. Control of nonlocal magnon spin transport via magnon drift currents. *Phys. Rev. Lett.* **126**, 257201 (2021).
54. Kalinikos, B. A. & Slavin, A. N. Theory of dipole-exchange spin wave spectrum for ferromagnetic films with mixed exchange boundary conditions. *J. Phys. C Solid State Phys.* **19**, 7013–7033 (1986).
55. de-la-Peña, S., Schlitz, R., Vélez, S., Cuevas, J. C. & Kamra, A. Theory of drift-enabled control in nonlocal magnon transport. *J. Phys.-Condens. Matter* **34**, 295801 (2022).
56. Garello, K. et al. Symmetry and magnitude of spin-orbit torques in ferromagnetic heterostructures. *Nat. Nanotechnol.* **8**, 587–593 (2013).
57. Klingler, S. et al. Measurements of the exchange stiffness of YIG films using broadband ferromagnetic resonance techniques. *J. Phys. D Appl. Phys.* **48**, 015001 (2014).

Acknowledgements

We acknowledge useful discussions with P. Noël and S. Vélez. Part of this work was supported by the Swiss National Science Foundation (Grant No. 200020_200465, P.G.) and by the Deutsche Forschungsgemeinschaft (DFG, German Research Foundation)–project numbers 529812702 (V.E.D.) and 425217212 (R.S. and M.L.).

Author contributions

R.S. performed the transport measurements and lithography, V.E.D. carried out the BLS characterization, and M.L. prepared the sample. R.S.

and V.E.D. analyzed the data with the help of S.O.D. R.S. and P.G. wrote the manuscript with the help of all coauthors. All authors discussed the results and commented on the manuscript.

Competing interests
The authors declare no competing interests.

Additional information
Supplementary information The online version contains supplementary material available at https://doi.org/10.1038/s41467-025-63350-0.

Correspondence and requests for materials should be addressed to Richard Schlitz.

Peer review information *Nature Communications* thanks Yumeng Yang and the other anonymous reviewer(s) for their contribution to the peer review of this work. A peer review file is available.